Supporting Online Information

Cooling history of the Pacific lithosphere

Michael H. Ritzwoller, Nikolai M. Shapiro, & Shi-Jie Zhong

Department of Physics, University of Colorado at Boulder, Boulder, CO 80309-0390 USA

Methods

Construction of the 3-D shear velocity and temperature models

The inversion for a radially anisotropic 3-D tomographic model of shear-wave velocity and temperature is performed in two steps. In the first step, we compiled a large new data set of broad-band group velocity measurements and produced Rayleigh and Love wave group velocity maps (1) on a $2° \times 2°$ grid across the Pacific from 18 sec period to 200 sec for Rayleigh waves and from 20 sec to 150 sec for Love waves. There are more than 200,000 measurement paths world-wide. We also constructed phase velocity maps using measurements compiled at Harvard (2) and Utrecht (3) Universities from 40 sec to 150 sec period. The great length of most wavepaths across the Pacific necessitates considering the path-length dependent spatial sensitivity of the surface waves in order to model wave-front healing and associated diffraction effects (1). The joint inversion of group and phase velocities gives better vertical resolution than either data type alone, providing unique information about the vertical variability of shear velocities in the uppermost mantle.

In the second step, the dispersion maps are used to construct a 3-D model on a $2° \times 2°$ grid to 400 km depth based on two separate parameterizations: a seismic parameterization (4) and a temperature parameterization derived from a thermal model (5). The seismic parameterization consists of 13 unknowns, seven in the crust and six in the mantle. The crust consists of three layers in which compressional (V_p) and shear (V_s) velocity are free variables as is crustal thickness; all seven crustal unknowns are perturbed from reference values taken from the model CRUST2.0 (G. Laske, personal communication, 2002). Isotropic mantle structure is parameterized with four radial cubic B-splines. The remaining two unknowns parameterize radial anisotropy. Because Rayleigh waves are predominantly sensitive to V_{sv} and Love waves to V_{sh}, we have constraints on only two of the five elastic moduli that describe a transversely isotropic medium. The basis functions for radial anisotropy represent the bifurcation of V_{sh} and V_{sv} in the uppermost mantle to a depth of

220 km and are sufficiently flexible to accommodate the unusual anisotropy in the Central Pacific
(2). The effective isotropic shear velocity, V_s, is defined as the average of the anisotropic velocities.

The inversion proceeds by Monte-Carlo sampling that walks randomly through a subspace of model space defined by a-priori constraints and forms a Markov-chain similar to Brownian motion. At each point on the $2° \times 2°$ grid, an ensemble of acceptable vertical profiles emerges (e.g., Fig. 2c,d in main text). The Monte-Carlo inversion estimates a range of seismic and temperature models at each depth so that only features that appear in every member of the ensemble of acceptable models are interpreted. We refer to these features as "persistent". When a single model is needed, we use the middle of the ensemble of acceptable models.

The temperature parameterization (Fig. 2b in main text) is based on a thermal model in which a thermally conductive layer (lithosphere) overlies a convective layer (asthenosphere) joined smoothly by a transition layer. The temperature profile within the conductive layer is described by the half-space cooling solution,

$$T(z) = T_s + (T_m - T_s) \; \mathrm{erf} \left(z/2\sqrt{\kappa\tau} \right), \tag{1}$$

where z is depth in the mantle, T_m is initial mantle temperature fixed at $1300°\mathrm{C}$, $T_s = 0°\mathrm{C}$ is the surface temperature, thermal diffusivity $\kappa = 1 \times 10^{-6}$ m^{2}s^{-1}, and τ is the "apparent thermal age" of the lithosphere. In the convective layer, the adiabatic temperature gradient $D_a = 0.5°\mathrm{C}$/km and the potential temperature T_p describe the thermal state of the asthenosphere.

Two mantle unknowns in the temperature parameterization specify the thermal state of the oceanic upper mantle: τ in the lithosphere and T_p in the underlying asthenosphere. These two unknowns replace the four B-splines in the seismic parameterization. The Monte-Carlo inversion with the temperature parameterization initiates in temperature space where a trial thermal model is constructed and is converted to shear velocity in the mantle, then trial seismic crustal structures are introduced as well as mantle radial anisotropy similar to the generation of these features in the seismic parameterization. The temperature profiles that fit the seismic data acceptably for an appropriate subset of seismic crustal models and models of radial anisotropy define the ensemble of acceptable profiles in temperature space and are also combined with the crustal and radial anisotropic models to define the ensemble of acceptable models in seismic velocity space.

Interconversion between temperature and shear velocity

Interconversion between temperature and shear velocity is based on laboratory-measured thermoelastic properties of mantle minerals represented as partial derivatives of the elastic moduli with respect to temperature, pressure, and composition (6). The compositional model for the oceanic upper mantle includes 75% Olivine, 21% Orthopyroxene, 3.5% Clinopyroxene, and 0.5% Spinel with

an Iron-to-Magnesium ratio of 10% (7). We compute shear velocity with the anelastic correction (6) from an anharmonic shear velocity, $v_{anel}(P, T, \omega) = v(P, T) \left[1 - \left(2Q_\mu^{-1}(P, T, \omega)/\tan(\pi a/2)\right)\right]$, using a temperature dependent Q-model, $Q_\mu(P, T, \omega) = A\omega^a \exp\left[a(H^* + PV^*)/RT\right]$, where R is the gas constant and we set the exponent $a = 0.15$, anelastic activation energy $H^* = 500$ kJ/mol, anelastic activation volume $V^* = 2.0 \times 10^{-5}$ m^3/mol, and the amplitude $A = 0.049$.

Half-Space Cooling (HSC) Model

The vertical temperature profile of the HSC model (8) is the solution to the one dimensional thermal diffusion equation for an infinite half-space, which takes the same form as equation (1). In contrast with the temperature parameterization for the seismic inversion, the error-function temperature profile for the HSC model continues infinitely with depth and explicitly does not include adiabatic heating. Predictions from the HSC model are intended to represent age trends expected for purely diffusive cooling. Several ad-hoc choices (e.g., T_m, the Q-model) in specifying the HSC model create uncertainty in the absolute level of temperatures and seismic velocities in the mantle. We account for this in Figures 1 and 3c-e in the main text, by shifting the HSC predictions to fit the observations optimally between 10 Ma and 60 Ma. This shift also approximately corrects for the effect of adiabatic heating.

Simulating Thermal Boundary Layer Instabilities

Our 3-D Cartesian convection model uses a depth- and temperature-dependent Arrhenius rheology with flow-through boundary conditions (9). The model box is 1000 km deep, 12,000 km long (in the direction of plate motion), and 3,000 km wide. At the surface, temperature is $0°$C and plate velocity is 5 cm/year, while at the bottom of the box temperature is $1350°$C and velocity is zero. The inflow boundary has temperatures corresponding to 10 Ma old lithosphere with velocities derived from a Couette flow. The outflow boundary has zero vertical temperature gradient and the same velocities as the inflow. The other two sidewalls (i.e., parallel to plate motion) have reflecting boundary conditions. The viscosity law is $\eta(z, T) = \eta_0(z) \exp(E/RT)$ where the pre-factor $\eta_0(z)$ is constant above 400 km depth and increases by a factor of 19 and 190 in the transition zone and lower mantle, respectively, compared with that in the upper mantle (10). The viscosity in the upper mantle is about 4×10^{19} Pa-s and rheological activation energy is 120 KJ/mol. This leads to $\sim$70 Ma onset time for TBI (10). This activation energy is consistent with that inferred from the study of flexural deformation near seamounts (11). Because we employ a Newtonian rheology, however, the activation energy may be viewed only as an "effective" rheological parameter for the mantle with a non-Newtonian rheology (12). The models are computed to a statistical steady-state. Other

model parameters are thermal diffusivity of 10^{-6} m^2/s, coefficient of thermal expansion of 3×10^{-5} K^{-1}, mantle density of 3,300 kg/m^3, and gravitational acceleration equal to 9.8 m/s^2.

Figure 1a shows the temperature profile from the 3-D convection simulation of thermal boundary layer instabilities (TBI) that is used to compute the thick solid line in Figure 4d of the main text. The heating of the lithosphere by the TBI is seen in the divergence of the isotherms from the predictions of the HSC model. The difference between lithospheric thermal structure in the TBI simulation and the HSC model is shown in Figure 1b, illustrating how TBI heats the lithosphere and cools the asthenosphere.

Related Results from the Seismic Parameterization

Similar trends in seismic velocities and temperatures are revealed in both the seismic and thermal parameterizations. In the main text, we show results using the temperature parameterization based on a thermal model only. Figures 2 and 3 here display aspects of the 3-D seismic and temperature models estimated with the seismic parameterization. These figures are to be contrasted with Figures 3 and 4 in the main text. Although there are subtle differences between the seismic and temperature models that are estimated with these two different parameterizations, the general features and age trends are similar, particularly the trend of apparent thermal age shown in Figure 4 in the main text. We estimate apparent thermal age from the seismic parameterization by converting V_s to temperature and fitting the thermal model shown in Figure 2b in the main text to the temperature profile. This results in a range of apparent thermal age (τ) and potential temperature (T_p) estimates that define the ensemble of acceptable temperature models. We use the middle of the ensemble to construct Figure 3.

Reheating inferred in the Central Pacific is absent in the lithosphere beneath the Atlantic and Indian Oceans. Figure 4 shows the average temperature structure beneath the other oceans worldwide where there are lithospheric age estimates (13). The isotherms are not observed to flatten between 70-100 Ma, in contrast with the temperature structure of the Pacific lithosphere shown in Figure 4e in the main text. The processes that reheat the lithosphere in the Central Pacific have not affected the lithosphere beneath other oceans similarly, at least not in the age range between 70-100 Ma.

References

1. Ritzwoller, M.H., Shapiro, N.M., Barmin, M.P., & Levshin, A.L., Global surface wave diffraction tomography, J. Geophys. Res., 107(B12), 233 (2003).

2. Ekström, G. & Dziewonski, A.M., The unique anisotropy of the Pacific upper mantle, *Nature*, 394, 168 (1998).

3. Trampert, J. & Woodhouse, J.H., Global phase velocity maps of Love and Rayleigh waves between 40 and 150 s period, *Geophys. J. Int.*, 122, 675 (1995).

4. Shapiro, N.M. & Ritzwoller, M.H., Monte-Carlo inversion for a global shear velocity model of the crust and upper mantle, Geophys. J. Int., 51, 88 (2002).

5. Shapiro, N.M. & Ritzwoller, M.H., Thermodynamic constraints on seismic inversions, Geophys. J. Int., submitted (2003).

6. Goes, S., Govers, R., & Vacher, R., Shallow mantle temperatures under Europe from P and S wave tomography, J. Geophys. Res., 105, 11,153 (2000).

7. McDonough, W.F. & Rudnick, R.L., Mineralogy and composition of the upper mantle, in: Ultrahigh-pressure mineralogy: physics and chemistry of the Earth's deep interior, R.J. Hemley, Editor, 139, Mineralogical Society of America, Washington, DC (1998).

8. Parker, R.L. & Oldenburg, D.W., Thermal model of ocean ridges, Nature Phys. Sci., 242, 137 (1973).

9. van Hunen, J., Huang, J., & Zhong, S., The effect of shearing on onset and vigor of small-scale convection with a Newtonian rheology, Geophys. Res., 30, doi:10.1029/2003GL018101 (2003).

10. Huang, J., Zhong, S. & van Hunen, J. Controls on sub-lithospheric small-scale convection, J. Geophys. Res., 108, doi:10.1029/2003JB002456 (2003).

11. Watts, A.B. & Zhong, S., Observations of flexure and the rheology of oceanic lithosphere, Geophys. J. Int., 142, 855 (2000).

12. Christensen, U. R., Convection with pressure and temperature dependent non-Newtonian rheology, Geophys. J. R. Astron. Soc., 77, 242 (1984).

13. Mueller, R.D., Roest, W.R., Royer, J.-Y., Gahagan, L.M., & Sclater, J.G., Digital isochrons of the world's ocean floor, J. Geophys. Res., 102, 3211 (1997).
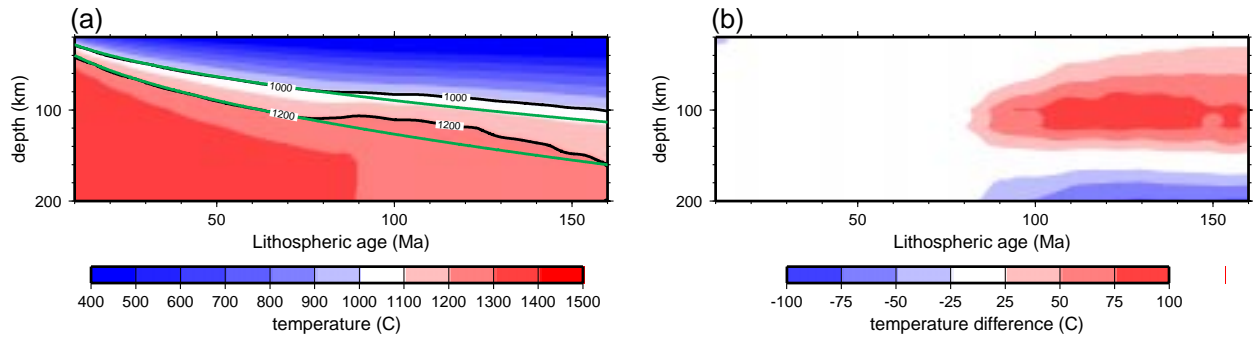
Figure 1: **Thermal structure versus lithospheric age for the simulation of TBI.** (a) Temperatures from the 3-D convection simulation of thermal boundary layer instabilities are averaged parallel to the ridge at each depth and plotted versus lithospheric age. The green lines are isotherms from the HSC model. (b) The difference between the temperatures from the simulation of TBI with the HSC model. Reds imply that temperatures in TBI simulation are warmer than in the HSC model.
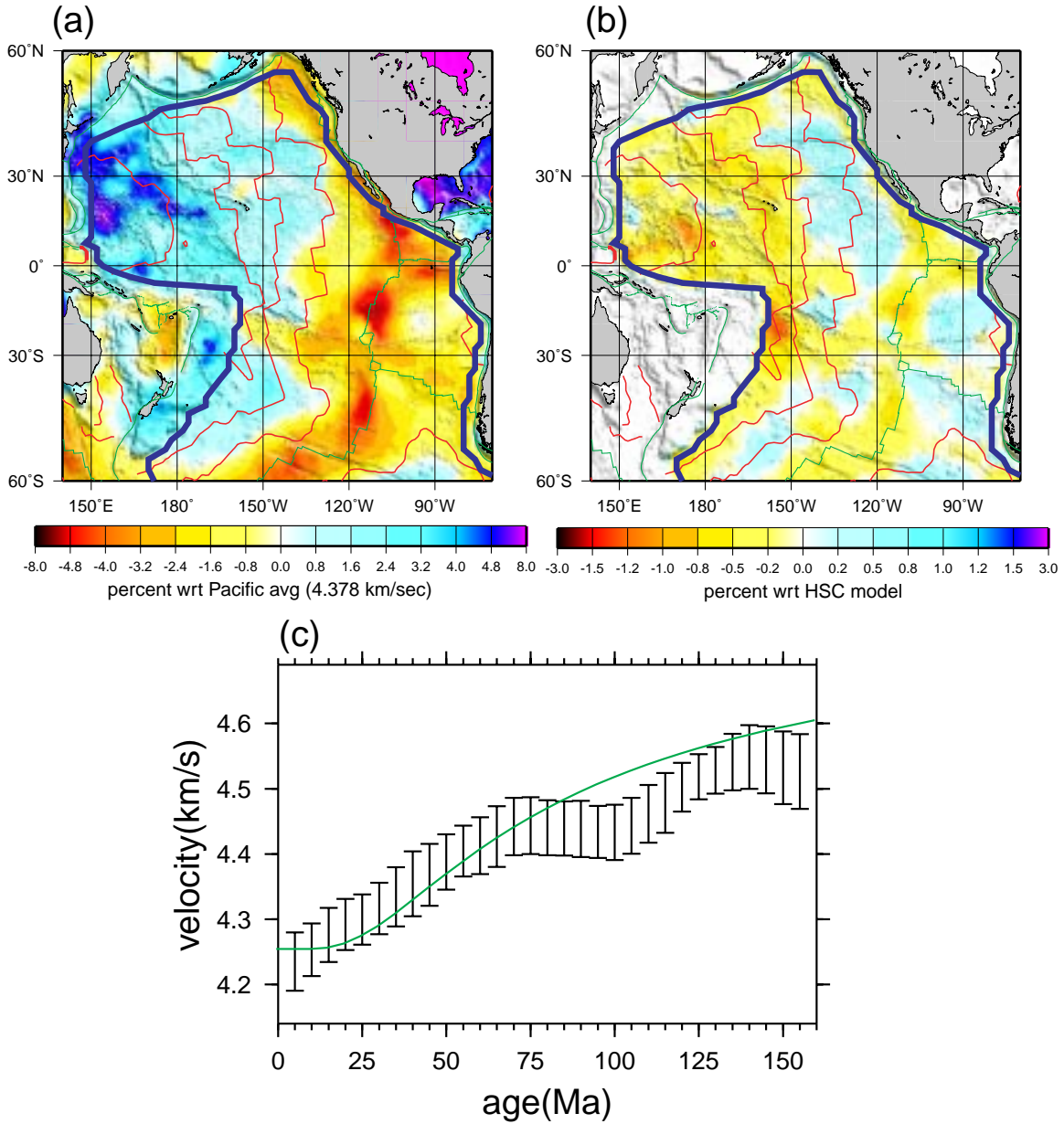
Figure 2: **Shear velocity structure of the Pacific upper mantle using the seismic parameterization and trend with lithospheric age.** (a) Isotropic shear velocity, V_s, at 100 km depth, as a perturbation to the average at this depth across the Pacific (4.378 km/sec). The green lines denote plate boundaries, the red lines are isochrons of lithospheric age in increments of 35 Ma, and the blue contour encloses the region where there are lithospheric age estimates (13). (b) V_s at 100 km depth presented as a perturbation to the prediction from the HSC model. (c) Shear velocity, averaged in 5 Ma lithospheric age bins across the Pacific, is plotted versus lithospheric age at 100 km depth. Error bars represent the standard deviation within each age range. The continuous green lines are the predictions from the HSC model shifted vertically the same amount as in the analogous figure in the main text: -30 m/s. This figure should be contrasted with the model derived using the temperature parameterization, Figure 3 in the main text.
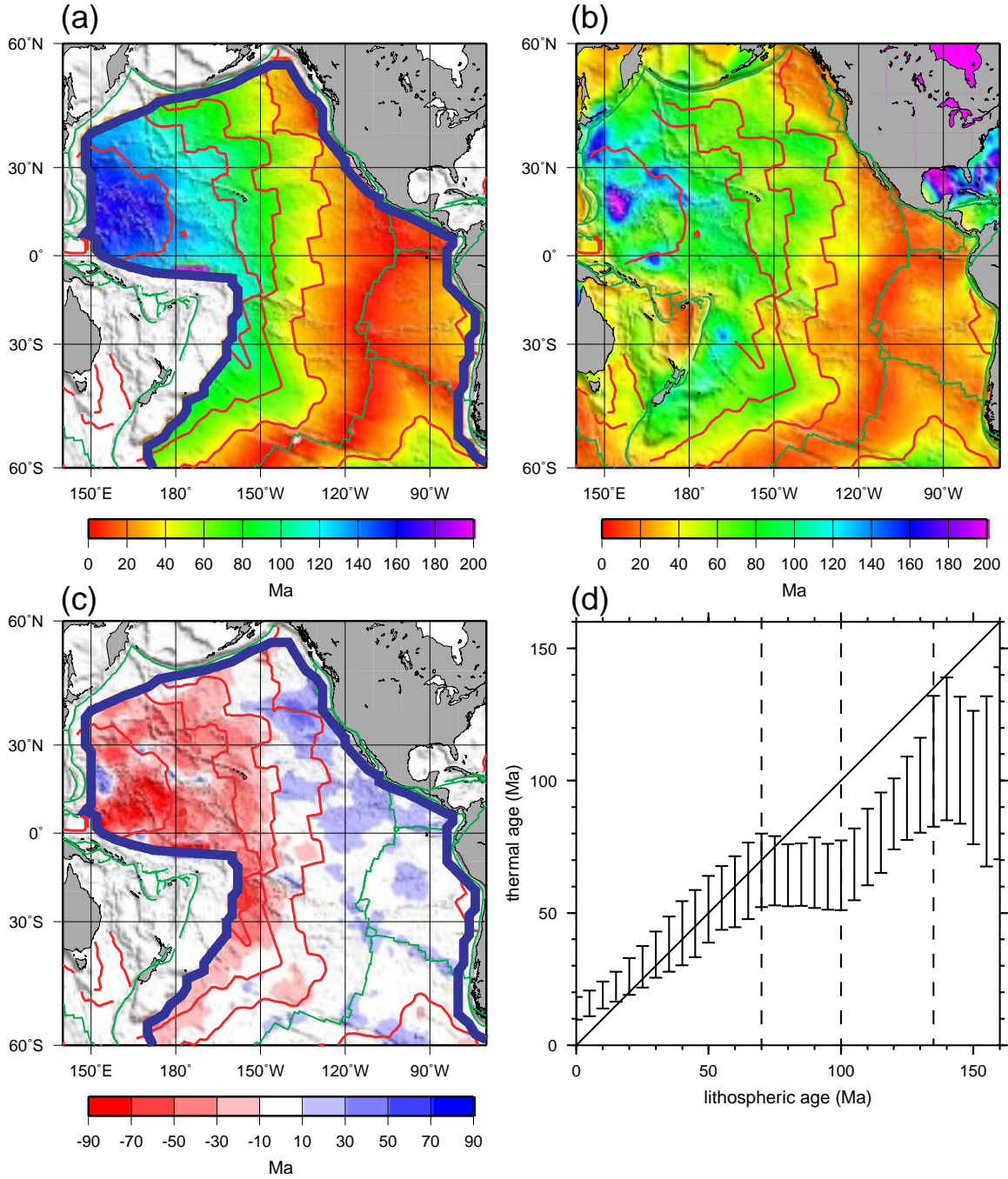
Figure 3: **Thermal age and age trend determined with the seismic parameterization.** (a) Lithospheric age in Ma, presented as a reference (13). (b) Apparent thermal age, τ, estimated with the seismic parameterization. (c) Difference between the lithospheric age and the apparent thermal age. Reds denote that the apparent thermal age is younger than the lithospheric age. In (a) - (c), the green, red, and blue lines are as in Figure 2a,b. (d) Comparison between apparent thermal age and lithospheric age. Apparent thermal age is averaged in 5 Ma lithospheric age bins across the Pacific and error bars represent the standard deviation within each age range. Contrast with Figures 3 and 4 in the main text, based on the thermal parameterization.
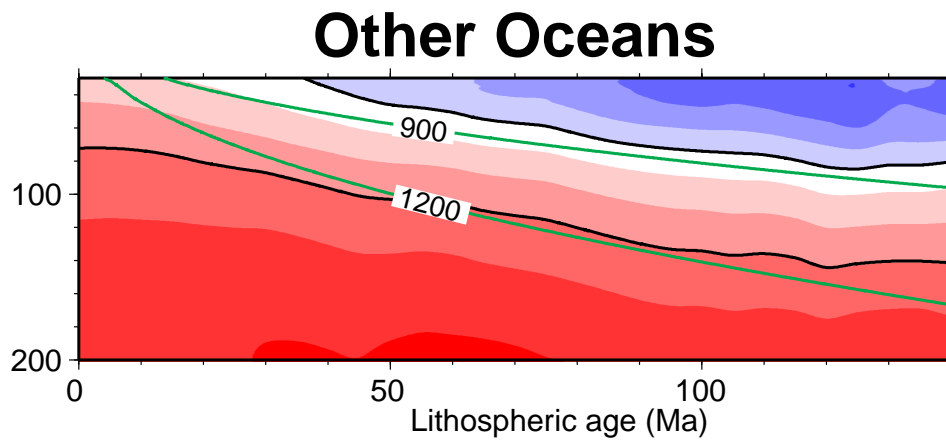
Figure 4: **Temperature in oceans other than the Pacific.** Upper mantle temperature averaged across all oceans other than the Pacific, plotted versus lithospheric age. Contrast Figure 4e in the main text. The green lines are isotherms from the HSC model.